Mon. Not. R. Astron. Soc. **384,** 1502–1510 (2008) doi:10.1111/j.1365-2966.2007.12807.x

Near-infrared evolution of brightest cluster galaxies in the most X-ray luminous clusters since $z = 1$

J. P. Stott,[1,2⋆] A. C. Edge,[1] G. P. Smith,[3,4] A. M. Swinbank[1] and H. Ebeling[5]

[1]*Institute for Computational Cosmology, Department of Physics, University of Durham, South Road, Durham DH1 3LE*
[2]*Astrophysics Research Institute, Liverpool John Moores University, Twelve Quays House, Egerton Wharf, Birkenhead CH41 1LD*
[3]*California Institute of Technology, Mail Code 105-24, Pasadena, CA 91125, USA*
[4]*School of Physics and Astronomy, University of Birmingham, Edgbaston, Birmingham B15 2TT*
[5]*Institute for Astronomy, 2680 Woodlawn Drive, Honolulu, HI 96822, USA*

Accepted 2007 November 29. Received 2007 November 28; in original form 2007 September 28

ABSTRACT

We investigate the near-infrared evolution of brightest cluster galaxies (BCGs) from a sample of rich galaxy clusters since $z \sim 1$. By employing an X-ray selection of $L_X > 10^{44}$ erg s^{-1}, we limit environmental effects by selecting BCGs in comparably high-density regions. We find a positive relationship between X-ray and near-infrared luminosity for BCGs in clusters with $L_X > 5 \times 10^{44}$ erg s^{-1}. Applying a correction for this relation, we reduce the scatter in the BCG absolute magnitude by a factor of 30 per cent. The near-infrared $J - K$ colour evolution demonstrates that the stellar population in BCGs has been in place since at least $z = 2$, and that we expect a shorter period of star formation than that predicted by current hierarchical merger models. We also confirm that there is a relationship between 'blue' $J - K$ colour and the presence of BCG emission lines associated with star formation in cooling flows.

Key words: galaxies: clusters: general – galaxies: elliptical and lenticular, cD – galaxies: evolution – cosmology: observations – infrared: galaxies.

1 INTRODUCTION

A brightest cluster galaxy (BCG) is a giant elliptical galaxy near the spatial and gravitational centre of a galaxy cluster. BCGs are the brightest and most massive stellar systems in the Universe. Their high luminosities and small scatter in absolute magnitude make them effective standard candles. As such they were originally used by astronomers to confirm and considerably increase the range of Hubble's redshift – distance law (e.g. Sandage 1972). BCGs are particularly important for galaxy formation and evolution studies as the above properties make them less prone to selection effects and biasing. Near-infrared (near-IR) photometry is often chosen for BCG studies as *K*-correction, stellar evolution and extinction by dust in this region of the spectrum are considerably less than at optical wavelengths.

There is considerable observational evidence that suggests giant ellipticals were formed at high redshift, and have been passively evolving to the present day (Bower, Lucey & Ellis 1992; Aragon-Salamanca et al. 1993; Stanford, Eisenhardt & Dickinson 1998; van Dokkum et al. 1998). Passive evolution describes a situation where the stellar population in a galaxy forms in a single burst at a redshift z_f. This population then matures, without further star formation. No evolution describes the case where the observed luminosity changes over cosmic time of a stellar population are purely attributed to the effects of distance and *K*-correction. Depending on the cluster selection technique, the BCG photometry can follow drastically different evolutionary tracks. For example, highly luminous X-ray clusters tend to prefer evolving models whereas low-L_X clusters are seen to have stellar populations preferring no evolution (Aragon-Salamanca, Baugh & Kauffmann 1998; Burke, Collins & Mann 2000; Nelson et al. 2002).

The latest hierarchical simulations of BCG formation predict that the stellar components of BCGs are formed very early (50 per cent at $z \sim 5$ and 80 per cent at $z \sim 3$, De Lucia & Blaizot 2007). This star formation occurs in separate subcomponents which then accrete to form the BCG through 'dry' mergers. It is important to note that in these simulations local BCGs are not directly descended from high-z ($z > 0.7$) BCGs. However, De Lucia & Blaizot (2007) find little physical difference between the progenitors of local BCGs and high-z BCGs or between the local BCGs and the descendants of the high-z BCGs. This means that observed evolution presented here can still be compared to simulation.

In this paper, we aim to test the above results and provide further constraints to simulations by comparing the K band and $J - K$ colour evolution of a well-defined X-ray selected sample of BCGs to a set of evolution models.

We study a large sample of the most X-ray luminous clusters known which correspond to the most extreme environments at their respective epochs. The motivation for studying an X-ray selected sample of clusters is to ensure that we are observing objects in similar high mass, high-density environments. This homogeneity is a key to our study as we wish to compare clusters over a range of redshifts. By incorporating clusters from the MAssive Cluster

⋆E-mail: jps@astro.livjm.ac.uk

Survey (MACS, Ebeling, Edge & Henry 2001), we are going to higher X-ray luminosity than any previous BCG study.

Λcold dark matter (CDM) cosmology ($\Omega_{\rm M} = 0.3$, $\Omega_{\rm Vac} = 0.7$, $H_0 = 70$) and the Vega magnitude system are used throughout.

2 DATA

2.1 The sample

To select BCGs in a homogeneous sample of massive clusters from $z = 0$–1, we require X-ray selected clusters from a number of large surveys. These clusters are all selected to have X-ray luminosities in excess of 10^{44} erg s^{-1} (0.1–2.4 keV), and therefore correspond to the most massive clusters known. The $z < 0.3$ sample is taken from the *ROentgen SATellite* (*ROSAT*) BCS, extended BCS (eBCS, Ebeling et al. 2000) and the X-ray Brightest Abell Clusters Survey (XBACS, Ebeling et al. 1996). We then select a comparable sample at $0.3 < z < 0.7$ from the MAssive Cluster Survey (MACS, Ebeling et al. 2001). Additional high-redshift clusters are sourced from analysis of archival observations of the clusters MS1054−0321 and RCS0224−0002. Details of the sample can be found in Tables A1, A2 and A3.

Our sample also contains four additional BCGs from spectroscopically confirmed $z \sim 0.9$ optical-IR selected clusters discovered in Swinbank et al. 2007. These BCGs where found in the UKIRT Infrared Deep Sky Survey (UKIDSS, Lawrence et al. 2007) and Deep eXtragalactic Survey (DXS, Survey Head: Alastair Edge). They are not yet confirmed as high-$L_{\rm X}$ clusters but they do have absolute magnitudes comparable with the rest of our sample (mean absolute magnitude of DXS BCGs is −26.6).

Fig. 1 shows the X-ray luminosity versus redshift for our sample which demonstrates that we are going to higher X-ray luminosity than any previous BCG study as we have excellent coverage in the $L_{\rm X} > 10^{45}$ erg s^{-1} range. In total we have a sample of 121 BCGs available for analysis of which 47 are in the $L_{\rm X} > 10^{45}$ erg s^{-1} regime compared to only seven from the Burke et al. (2000) sample.

2.2 Photometry

To study a sample of BCGs spanning such a wide-redshift range, we obtain data from several sources.

A combination of the Two-Micron All-Sky Survey (2MASS) extended and point source catalogues (Skrutskie et al. 2006) is used for the $z < 0.15$ BCS, eBCS and XBACS BCGs. The limiting magnitudes for the eXtended Source Catalogue (XSC) are $J = 15.1$ and $K_{\rm s} = 13.5$ mag. The XSC K20 fiducial elliptical total magnitudes are used throughout incorporating the same aperture size in both J and K bands which is crucial to ensure precise colour photometry.

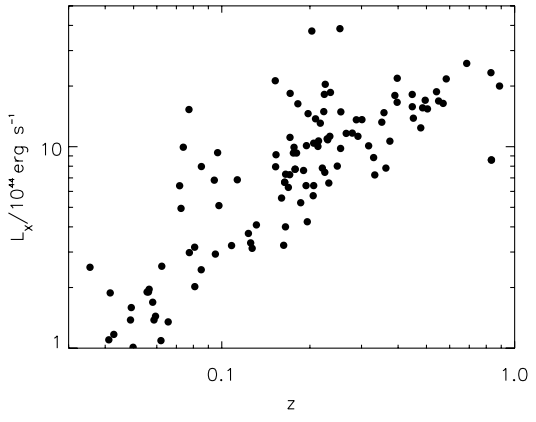

Figure 1. The X-ray luminosity versus z for our sample.

The $0.15 < z < 0.3$ BCS, eBCS and XBACS observations were performed in 2004 and 2005 in variable seeing (0.9–1.5 arcsec) with the Wide-field InfraRed Camera (WIRC, Wilson et al. 2003) instrument on the Palomar 200 arcsec Hale telescope. These data were reduced with the WIRCTASK IRAF scripts.

The $0.3 < z < 0.7$ MACS data are from three sources. Part of these data were obtained in 2002 in 0.4–0.7 arcsec seeing using the UKIRT Fast-Track Imager (UFTI) camera on the United Kingdom InfraRed Telescope (UKIRT). The data were reduced using the ORAC-DR pipeline. More MACS clusters were observed in ∼1.0 arcsec seeing in 2002 again with the WIRC instrument on the Palomar 200 arcsec Hale telescope. This was reduced with the WIRCTASK IRAF scripts. The remaining clusters were observed in 2004 (PI: J.-P. Kneib) in ∼0.6 arcsec seeing conditions using the Infrared Spectrometer And Array Camera (ISAAC) on the Very Large Telescope (VLT). These data were reduced with the ISAAC eclipse pipeline.

The high-redshift ($z > 0.7$) clusters MS1054−0321 and RCS0224−0002 are sourced from archival data. The MS1054−0321 data are from VLT/ISAAC observations obtained as part of the Faint InfraRed Extragalactic Survey (FIRES, Förster Schreiber et al. 2006), and the RCS0224−0002 cluster was observed using WIRC/Palomar.

We include additional high-redshift photometry from the literature. The near-IR selected $z \sim 0.9$ clusters are sourced from UKIDSS DXS data described in Swinbank et al. (2007) and reanalysed here to ensure homogeneity.

The BCG photometry for all of our $z > 0.15$ near-IR data is extracted using SExtractor's 'Best' magnitude (Bertin & Arnouts 1996), as used by Nelson et al. (2002), which is comparable to the 2MASS K20 fiducial elliptical magnitude (Elston et al. 2005). The centre of clusters can be very densely populated, so for crowded objects the 'Best' magnitude uses the isophotal magnitude which excludes the light from close neighbours and is therefore more reliable than a fixed aperture. The 'Best' magnitude is shown to be robust to galaxy shape as we find no trend between ellipticity of the aperture/BCG and the absolute K-band magnitude. It is important to note that the 'Best' magnitude may underestimate the integrated brightness by up to a tenth of a magnitude for BCGs at $K = 17.5$ (Martini 2001) which will be the dominant error in our high-redshift photometry. We run SExtractor in dual mode with the K-band apertures used to extract the J-band photometry to ensure good colour determination. The photometry calibration for our data was achieved with a combination of 2MASS and/or standard star observations.

The Wide-Angle *ROSAT* Pointed Surveys (WARPS, Scharf et al. 1997; Jones et al. 1998) X-ray selected $z \sim 0.9$ 'total' magnitude photometry was sourced from data described in Ellis & Jones (2004).

All magnitudes are corrected for Galactic extinction using Schlegel, Finkbeiner & Davis (1998). The typical extinction values for our clusters were in the range 0.01–0.04 mag in K.

3 ANALYSIS AND RESULTS

3.1 The BCG degree of dominance

We first look to see if differing cluster core environments effect our results. A measure of environment which can easily be

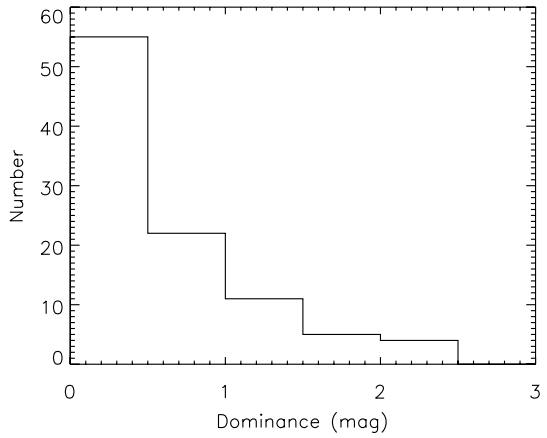

Figure 2. A histogram of the degree of BCG dominance for our sample.

extracted from photometric data is the degree of dominance. This parametrizes the difference in luminosity between the BCG and the next brightest galaxies in the cluster. The BCG may be the dominant elliptical in a cluster centre containing much smaller galaxies or it may be in a system where it is only marginally brighter than the next brightest members. The degree of dominance is defined as $\Delta\, m_{1-2,3} = (m_2 + m_3)/2 - m_1$ where m_1 is the magnitude of the BCG, and m_2 and m_3 are the magnitudes of the second and third brightest members, respectively, (Kim et al. 2002). The second and third brightest galaxies are selected as the next two brightest galaxies on the cluster red sequence within a radius of 500 kpc of the BCG. Taking the average of the second and third ranked galaxies is slightly more robust to contamination than just using the second. It also removes the weighting from cases where there are two BCG candidates that are far more luminous than the rest of the cluster. Fig. 2 shows a histogram of the distribution of the degree of K band dominance for our sample. The maximum cluster dominance found in our sample is 2.43 mag. We find that the majority of our BCGs are in cluster environments where they are not highly dominant. The key result is that we find no trend between dominance and redshift, X-ray luminosity or absolute K-band magnitude for our sample. We are therefore satisfied that the differing galaxy environment between cluster cores has no effect on the results presented in this paper.

3.2 *K*-band correction

To observe whether BCGs from the most X-ray luminous clusters can be considered as 'standard candles', we present the absolute K-band magnitude versus the X-ray luminosity (Fig. 3, left-hand panel). The absolute K magnitude was calculated using K and passive evolution corrections from a Bruzual & Charlot (2003) Spectral Energy Distribution with a simple stellar population (SSP), $z_f = 5$ and solar metallicity.

From the left-hand panel of Fig. 3, we find that there is no correlation between absolute magnitude and L_X below $L_X \sim 5 \times 10^{44}\,\mathrm{erg\,s^{-1}}$; however, beyond this value there appears to be a positive relationship. The strength of this correlation is found to be moderate with a Pearson correlation statistic $r = 0.46$. To demonstrate that this is not caused by a difference in the photometric technique between the high- and the low-redshift samples, we highlight the BCGs above and below the mean redshift ($z = 0.25$) which shows that the high- and the low-z BCGs in the trend region are well mixed.

Instead of a M_K correction with L_X, we could assume that the trend in Fig. 3 is caused by evolution with redshift as our clusters are increasingly more X-ray luminous at higher z (Fig. 1). If we do ascribe the trend to redshift then we require $\gtrsim$2 mag of passive evolution to provide the same M_K correction as that with L_X. This magnitude of passive evolution at $z = 1$ is not seen in stellar population models so we believe that our $M_K - L_X$ trend is real, and we concentrate on this for the remainder of the paper.

Previous works have also found that BCGs from higher L_X clusters are brighter in the K band (Collins & Mann 1998; Brough et al. 2005). Observations suggest that BCGs in higher mass systems assemble their stellar mass earlier, and are therefore brighter than those from less massive clusters (Brough et al. 2005). This is qualitatively consistent with theories of hierarchical assembly.

We quantify the trend with a two parameter χ^2 minimized fit to the $L_X > 5 \times 10^{44}\,\mathrm{erg\,s^{-1}}$ BCGs. This lower L_X limit is chosen as this is the value where the high-L_X trend with M_K intersects with the median M_K value of the low-L_X BCGs. The gradient of this fit is found to be -1.1 ± 0.3 mag per decade of X-ray luminosity. We then use this fit to correct for the effect of L_X on the magnitude, shown in the right-hand panel of Fig. 3. In Fig. 4, we plot the 1σ dispersion in the absolute magnitude versus z for both the corrected and the uncorrected samples. From this we can see that the applied correction reduces the scatter by a factor of $\sim$30 per cent.

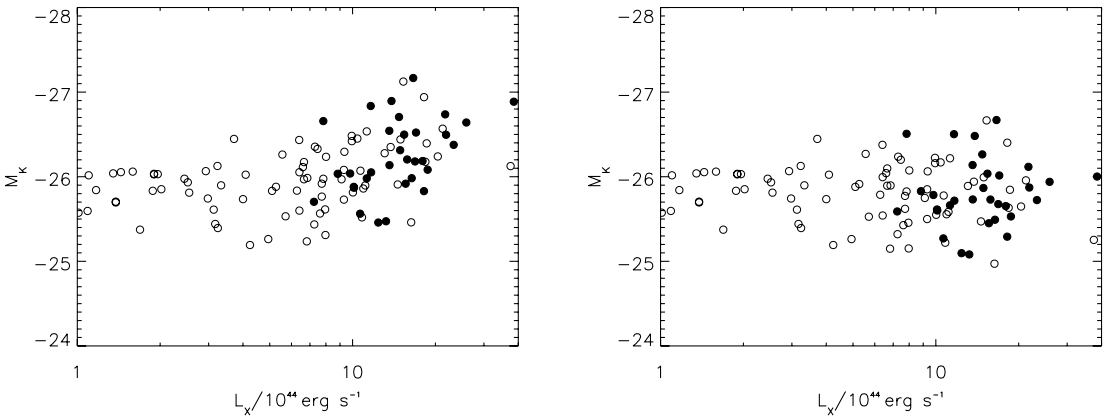

Figure 3. Left-hand panel: absolute K-band magnitude versus X-ray luminosity. The unfilled and filled points are BCGs below and above the mean redshift of the sample ($z = 0.25$), respectively. Right-hand panel: the L_X corrected absolute K-band magnitude versus X-ray luminosity.

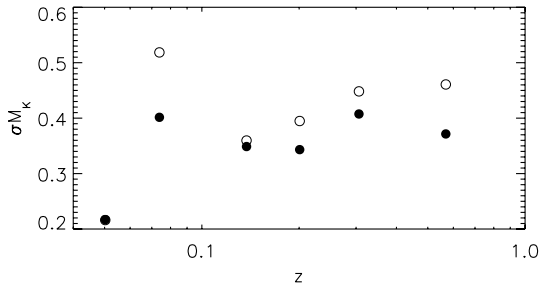

Figure 4. The 1σ dispersion in absolute K-band magnitude versus redshift. The filled/unfilled points are for the corrected/uncorrected M_K values.

The mean absolute K-band magnitude for the L_X corrected cluster sample is -25.81 ± 0.35 compared to a mean M_K of -26.23 ± 0.45 mag for the uncorrected K-band data. The mean magnitude of our sample is therefore comparable to the -26.40 ± 0.47 mag of Collins & Mann (1998). For comparison with simulation, De Lucia & Blaizot (2007) find their mean $M_K = -26.6 \pm 0.16$ mag which, although brighter, is within 1σ of our uncorrected mean. This demonstrates that the results from our findings can be compared to the work of both Collins & Mann (1998) and De Lucia & Blaizot (2007).

3.3 Hubble diagram

Now we are satisfied that we have limited environmental effects within our sample, we can test the nature of the BCG evolution. The Hubble diagram probes both the build up of mass and stellar evolution of the BCGs. Fig. 5 shows the uncorrected and X-ray luminosity corrected K-band Hubble diagrams for the whole BCG sample, respectively. The uncorrected Hubble diagram is included for comparison to demonstrate the success of the L_X – magnitude correction introduced in Section 3.2.

The lines plotted represent various stellar population models from the Bruzual & Charlot (2003) GALAXEV code. All models assume a Salpeter initial mass function (IMF) (Salpeter 1955) and solar metallicity (Humphrey & Buote 2006). The models are normalized to the median BCG magnitude at $z \lesssim 0.1$. The formation redshifts of $z_f = 5$, 2 and a no evolution model are chosen for comparison with Burke et al. (2000).

By measuring the residuals about each model track in the corrected Hubble diagram, we can identify which scenario best describes the data. Fig. 6 shows these residuals. The rms scatters about the three models are 0.44, 0.41 and 0.40 for the no evolution, $z_f = 2$ and 5 passive evolution models, respectively. We find that the passive evolution models provide a better description than no evolution in agreement with the observations of Burke et al. (2000) and the simulations of De Lucia & Blaizot (2007).

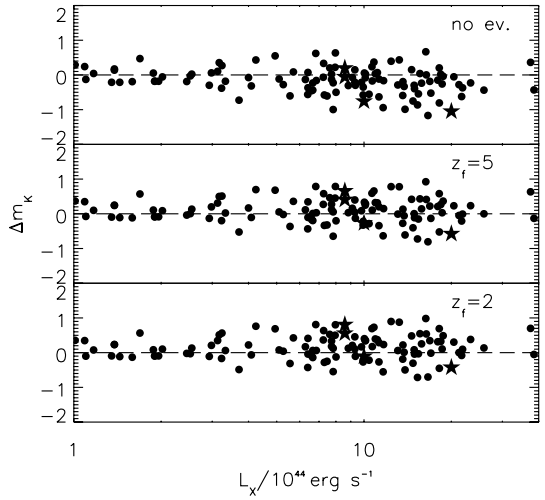

Figure 6. The residuals of the BCG corrected m_K about the non-evolution and the $z_f = 5$ and 2 passive evolution models from Fig. 5. $\Delta m_K = m_{BCG} - m_{model}$. The stars represent the WARPS BCGs.

As the significance of this result is low, and there is some uncertainty over the validity of the $M_K - L_X$ correction, we look to further constrain the evolution of BCGs by investigating $J - K$ colour evolution with redshift in Section 3.4.

3.4 Colour evolution with redshift

Most BCG studies concentrate on the K-band evolution with redshift but here we introduce the J band to observe the evolution of the $J - K$ colour, which probes the stellar evolution of our sample. Fig. 7 is the $J - K$ colour versus z for our BCG sample. As in Section 3.3 the models we compare to are calculated using the Bruzual & Charlot (2003) GALAXEV codes. These models assume a Salpeter IMF and solar metallicity.

In addition, the dash dot line represents the model from De Lucia & Blaizot (2007). This model forms 50 per cent of the BCG stellar content by $z \sim 5$ and 80 per cent by $z \sim 3$. We calculate that

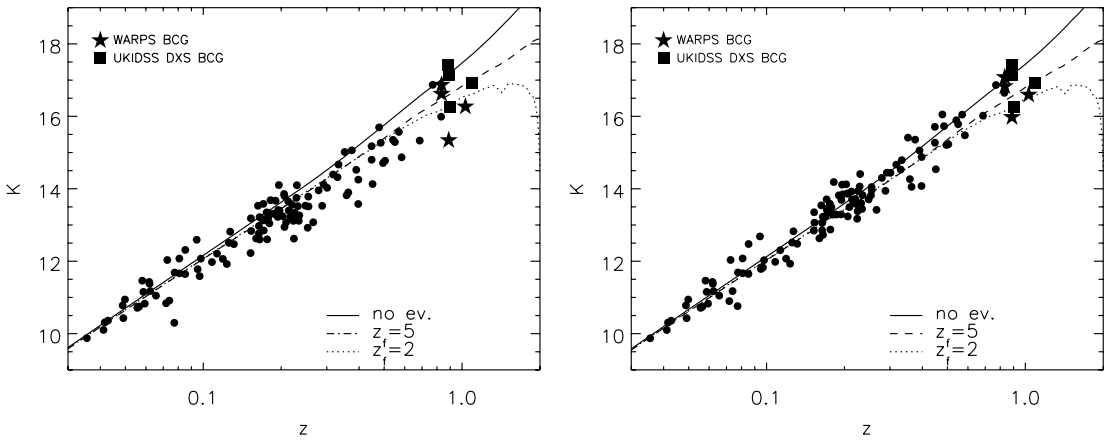

Figure 5. Left-hand panel: K versus z Hubble diagram for the entire BCG sample. The lines represent different models from the Bruzual & Charlot (2003) GALAXEV codes. All models assume a Salpeter IMF and solar metallicity. Right-hand side: the corrected K versus z Hubble diagram for the entire BCG sample.

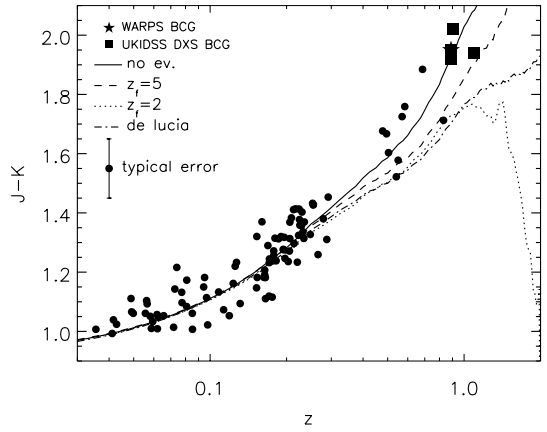

Figure 7. $J - K$ versus z for the entire BCG sample. The Lines represent different models from the Bruzual & Charlot (2003) GALAXEV codes and the hierarchical merger model of De Lucia & Blaizot (2007). All of the GALAXEV models assume a Salpeter IMF and Solar metallicity. The De Lucia & Blaizot (2007) model forms 50 per cent of the BCG stellar content by $z \sim 5$ and 80 per cent by $z \sim 3$ with a Chabrier IMF. The WARPS BCG with J-band data is from the cluster ClJ1226.9+3332.

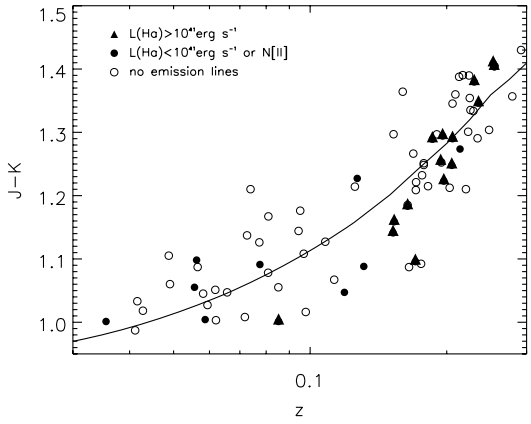

Figure 8. $J - K$ versus z for BCGs with spectral information normalized to the solid non-evolution line from Fig. 7.

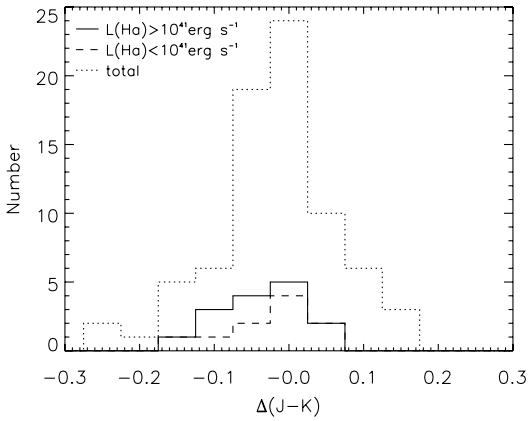

Figure 9. This is the histogram of the BCG distribution about the no evolution line. Negative values are bluewards of the no evolution line, positive values are redwards.

this corresponds to an exponentially decreasing star formation rate with an e-folding time $\tau \sim 0.93$ Gyr. For consistency, we calculate this photometric model using the same population synthesis as De Lucia & Blaizot (2007), a Bruzual & Charlot (2003) model with a Chabrier (2003) IMF.

The data show no real preference for a particular evolution track up to $z \sim 0.4$ as the models show little divergence up to this point. However, beyond this redshift the ISAAC, UKIDSS DXS and WARPS BCGs appear to favour the no evolution or passive $z_f = 5$ models over $z_f = 2$. We quantify this for the redshift range $0.8 < z < 1$ by comparing the mean $J - K$ colour to the model values. We find a formation redshift $z_f = 2$ is ruled out to a significance of 6σ while the $z_f = 5$ and no evolution models are both within 3σ of the mean BCG colour. These results are in agreement with both the observations of Burke et al. (2000) who favour $z_f > 5$ and the no evolution result of Aragon-Salamanca et al. (1998). The De Lucia & Blaizot (2007) model is shown to be in good agreement with our observations at low z but becomes too blue compared to our current high-z data, suggesting its star formation lasts for too long. We calculate that this model would provide a better description to our data if it had an exponentially decreasing star formation rate with e-folding time $\tau \sim 0.5$ Gyr.

3.5 Emission lines

With the unprecedented wealth of colour information available for our sample in combination with spectroscopy from Crawford et al. (1999), we can investigate the subpopulation of BCGs that have line emission. This emission originates from star-forming activity attributed to cooling flows (see review by Fabian 1994). In this process, intracluster gas cooling near the cluster centre accretes on to the BCG where it can trigger star formation and therefore line emission.

BCGs with the most luminous line emission [$L(\mathrm{H}\alpha) > 10^{41}$ erg s^{-1}] are found to have a significantly bluer continuum, and therefore a bluer optical colour than those with less or no line emission (Crawford et al. 1999). Here, we look for this same trend in the near-IR colour which may aid selection of high-redshift cooling flow clusters for future studies.

The Crawford et al. (1999) table of the *ROSAT* BCS (Ebeling et al. 2000) contains BCG emission-line data for all of the members of the BCS sample. This information is included in our $J - K$ versus z plot to see if there is any trend between line emission and near-IR colour (Fig. 8). For this plot, the sample has been normalized to fit the $J - K$ non-evolution track from Fig. 7 to ensure there are no errors due to an unknown colour term.

Fig. 9 shows a histogram of the BCG distribution about the no evolution line in Fig. 8. Negative values are bluewards of the model and positive values are redwards. The figure shows that we find both our high- [$L(\mathrm{H}\alpha) > 10^{41}$ erg s^{-1}] and low-luminosity Hα emitting BCG, populations have a peak in the centre and then a blue tail. This is also seen in optical studies which find a Gaussian around the zero position and a number of populated bins tailing off on the blue side (e.g. Courtney 2003). We can therefore say that we do find a correspondence between the presence of BCG Hα emission lines and blue near-IR colour. In addition, we find no correlation between the presence of line emission and the BCG degree of dominance.

4 SUMMARY

We have studied the evolution and environment of BCGs in the most X-ray luminous clusters since $z \sim 1$.

We find a positive relationship between the near-IR luminosity of the BCG and the X-ray luminosity of its host cluster for

clusters where $L_X > 5 \times 10^{44}\,\mathrm{erg\,s^{-1}}$. Previous studies have lacked the sample coverage of this work in the high-L_X regime required to observe this trend. When a correction for this M_K–L_X relation is applied the scatter in the BCG absolute magnitude is reduced.

The K-band Hubble diagram for the corrected sample is shown to follow passive evolution. This result is in agreement with the observations of Burke et al. (2000) and the simulations of De Lucia & Blaizot (2007).

To improve the constraints on BCG evolution, we include J-band photometry allowing us to compare the $J - K$ colour versus redshift to a set of evolution models. We find that the high-redshift BCGs from our MACS, UKIDSS DXS and WARPS data appear to rule out passive evolution with a formation redshift less than two. We therefore expect that the stellar population of BCGs has been in place since at least redshift two, in agreement with the observations of Burke et al. (2000). For comparison with simulation, the De Lucia & Blaizot (2007) model (50 per cent stellar content in place by $z \sim 5$ and 80 per cent in place by $z \sim 3$) provides a good description to our observations at low z but is too blue compared to our current high-z data. This suggests that the simulated BCGs form stars for a longer time period than the observed BCGs. We look to confirm this result in the future with additional high-redshift data.

When studying the spectra of individual BCGs, we observe a correlation between blue near-IR colour and the presence of high-luminosity [$L(\mathrm{H}\alpha) > 10^{41}\,\mathrm{erg\,s^{-1}}$] emission lines. Fig. 9 shows that such emission-line BCGs mainly lie on the blue side of the near-IR colour distribution. This has been seen previously in optical studies (Courtney 2003), and will be a useful tool in concert with X-ray observations for selecting high-redshift cooling flow clusters.

In conclusion, we confirm that near-IR BCG photometry is a valuable tool for probing the evolution of the bright end of the cluster red sequence. When taken in conjunction with faint end studies (e.g. Stott et al. 2007), we can begin to build up a unified picture of cluster evolution where the bright end has been in place since high redshift while the red sequence is being built up over cosmic time by in falling or transforming galaxies.

ACKNOWLEDGMENTS

We thank the referee for their useful comments which have improved the clarity of this paper.

We also thank Carlton Baugh, Richard Bower and Sarah Brough for useful discussions. JPS acknowledges support through a Particle Physics and Astronomy Research Council Studentship. GPS acknowledges financial support from the Royal Society.

This publication makes use of data products from the Two-Micron All-Sky Survey, which is a joint project of the University of Massachusetts and the IR Processing and Analysis Centre/California Institute of Technology, funded by the National Aeronautics and Space Administration and the National Science Foundation.

This work is based in part on data obtained as part of the UKIRT Infrared Deep Sky Survey.

The United Kingdom Infrared Telescope is operated by the Joint Astronomy Centre on behalf of the Science and Technology Facilities Council of the United Kingdom.

This work is based partly on observations obtained at the Hale 200-inch telescope at Palomar Observatory.

REFERENCES

Aragon-Salamanca A., Ellis R. S., Couch W. J., Carter D., 1993, MNRAS, 262, 764
Aragon-Salamanca A., Baugh C. M., Kauffmann G., 1998, MNRAS, 297, 427
Bertin E., Arnouts S., 1996, A&AS, 117, 393
Bower R. G., Lucey J. R., Ellis R. S., 1992, MNRAS, 254, 589
Brough S., Collins C. A., Burke D. J., Lynam P. D., Mann R. G., 2005, MNRAS, 364, 1354
Bruzual G., Charlot S., 2003, MNRAS, 344, 1000
Burke D. J., Collins C. A., Mann R. G., 2000, ApJ, 532, L105
Chabrier G., 2003, PASP, 115, 763
Collins C. A., Mann R. G., 1998, MNRAS, 297, 128
Courtney N. J. D., 2003, PhD thesis, Durham Univ.
Crawford C. S., Allen S. W., Ebeling H., Edge A. C., Fabian A. C., 1999, MNRAS, 306, 857
De Lucia G., Blaizot J., 2007, MNRAS, 375, 2
Ebeling H., Voges W., Bohringer H., Edge A. C., Huchra J. P., Briel U. G., 1996, MNRAS, 281, 799
Ebeling H., Edge A. C., Allen S. W., Crawford C. S., Fabian A. C., Huchra J. P., 2000, MNRAS, 318, 333
Ebeling H., Edge A. C., Henry J. P., 2001, ApJ, 553, 668
Ellis S. C., Jones L. R., 2004, MNRAS, 348, 165
Elston R. J. et al., 2005, ApJ, 639, 816
Fabian A. C., 1994, ARA&A, 32, 277
Förster Schreiber N. M. et al., 2006, AJ, 131, 1891
Humphrey P. J., Buote D. A., 2006, ApJ, 639, 136
Jones L. R., Scharf C., Ebeling H., Perlman E., Wegner G., Malkan M., Horner D., 1998, ApJ, 495, 100
Kim R. S. J., Annis J., Strauss M. A., Lupton R. H., 2002, in Borgani S., Mezzetti M., Valdarnini R., eds, ASP Conf. Ser. Vol. 268, Tracing Cosmic Evolution with Galaxy Clusters. Astron. Soc. Pac., San Francisco, p. 395
Lawrence A. et al., 2007, MNRAS, 379, 1599
Martini P., 2001, AJ, 121, 598
Nelson A. E., Gonzalez A. H., Zaritsky D., Dalcanton J. J., 2002, ApJ, 566, 103
Salpeter E. E., 1955, ApJ, 121, 161
Sandage A. R., 1972, ApJ, 173, 585
Scharf C. A., Jones L. R., Ebeling H., Perlman E., Malkan M., Wegner G., 1997, ApJ, 477, 79
Schlegel D. J., Finkbeiner D. P., Davis M., 1998, ApJ, 500, 525
Skrutskie M. F. et al., 2006, AJ, 131, 1163
Stanford S. A., Eisenhardt P. R., Dickinson M., 1998, ApJ, 492, 461
Stott J. P., Smail I., Edge A. C., Ebeling H., Smith G. P., Kneib J.-P., Pimbblet K. A., 2007, ApJ, 661, 95
Swinbank A. M. et al., 2007, MNRAS, 379, 1343
van Dokkum P. G., Franx M., Kelson D. D., Illingworth G. D., 1998, ApJ, 504, L17
Wilson J. C. et al., 2003, in Masanori I., Moorwood A. F. M., eds, Proc. SPIE Vol. 4841, Instrument Design and Performance for Optical/Infrared Ground-based Telescopes. SPIE, Bellingham, p. 451

APPENDIX A: THE BCG SAMPLE

Table A1. The $z \lesssim 0.15$ 2MASS BCGs. † denotes presence of H_α emission. y: H_α emission, n: no H_α emission.

Cluster	RA	Dec. (J2000)	z	J	K	M_K	L_X (10^{44} erg s^{-1})	$H_\alpha^\dagger$
Abell 1902	14:21:40.53	+37:17:31.0	0.160	14.00	12.63	−26.26	5.56	n
Abell 193	01:25:07.62	+08:41:57.6	0.049	11.49	10.43	−26.06	1.59	n
Abell 1930	14:32:37.96	+31:38:48.9	0.131	13.57	12.47	−26.02	4.09	y
Abell 1991	14:54:31.48	+18:38:32.5	0.059	12.16	11.15	−25.71	1.38	y
Abell 2029	15:10:56.13	+05:44:42.4	0.077	11.43	10.30	−27.12	15.29	n
Abell 2034	15:10:11.71	+33:29:11.2	0.113	13.28	12.21	−25.99	6.85	n
Abell 2052	15:16:44.49	+07:01:17.7	0.035	10.88	9.88	−25.93	2.52	y
Abell 2065	15:22:24.02	+27:42:51.7	0.073	13.18	12.03	−25.26	4.94	n
Abell 2072	15:25:48.66	+18:14:09.5	0.127	14.05	12.82	−25.61	3.13	y
Abell 2107	15:39:39.05	+21:46:57.9	0.041	11.10	10.10	−26.02	1.10	n
Abell 2124	15:44:59.03	+36:06:34.1	0.066	12.10	11.05	−26.04	1.35	n
Abell 2175	16:20:31.14	+29:53:27.5	0.095	12.96	11.78	−26.07	2.93	n
Abell 2204	16:32:46.71	+05:34:30.9	0.152	13.37	12.23	−26.57	21.25	y
Abell 2244	17:02:42.50	+34:03:36.7	0.097	12.70	11.59	−26.29	9.34	n
Abell 2259	17:20:09.65	+27:40:07.9	0.164	13.96	12.77	−26.17	6.66	n
Abell 2292	17:57:06.69	+53:51:37.5	0.119	13.12	12.06	−26.24	0.73	y
Abell 2345	21:27:13.72	−12:09:46.3	0.177	13.84	12.60	−26.48	9.93	n
Abell 2377	21:45:57.12	−10:06:18.7	0.081	13.16	12.07	−25.44	3.17	n
Abell 2382	21:51:55.63	−15:42:21.6	0.062	12.49	11.43	−25.54	0.91	n
Abell 2384	21:52:21.97	−19:32:48.6	0.094	13.74	12.59	−25.24	6.82	n
Abell 2402	21:58:28.89	−09:47:49.7	0.081	12.84	11.67	−25.85	2.02	n
Abell 2415	22:05:35.49	−05:32:09.7	0.058	12.51	11.46	−25.37	1.69	n
Abell 2426	22:14:31.59	−10:22:26.3	0.098	13.09	12.07	−25.83	5.10	n
Abell 2428	22:16:15.60	−09:19:59.7	0.085	12.71	11.64	−25.98	2.45	n
Abell 2443	22:26:07.93	+17:21:23.5	0.108	13.11	11.98	−26.13	3.23	n
Abell 2457	22:35:40.80	+01:29:05.6	0.059	11.86	10.83	−26.05	1.44	n
Abell 2495	22:50:19.73	+10:54:12.8	0.078	12.78	11.69	−25.74	2.98	y
Abell 2496	22:50:55.85	−16:24:22.0	0.123	13.09	11.92	−26.45	3.71	n
Abell 2589	23:23:57.45	+16:46:38.1	0.042	11.35	10.31	−25.83	1.88	n
Abell 2593	23:24:20.09	+14:38:49.7	0.043	11.38	10.36	−25.84	1.17	n
Abell 2597	23:25:19.72	−12:07:27.0	0.085	13.32	12.31	−25.31	7.97	y
Abell 2622	23:35:01.50	+27:22:20.5	0.062	12.39	11.38	−25.60	1.09	n
Abell 2626	23:36:30.59	+21:08:49.8	0.057	11.84	10.75	−26.03	1.96	n
Abell 2627	23:36:42.10	+23:55:29.1	0.126	13.73	12.51	−25.90	3.33	n
Abell 2665	22:50:50.56	+06:08:58.9	0.056	11.85	10.74	−26.03	1.90	y
Abell 2717	00:03:12.98	−35:56:13.6	0.050	12.00	10.94	−25.57	1.01	n
Abell 2734	00:11:21.66	−28:51:15.5	0.062	12.22	11.17	−25.81	2.55	y
Abell 376	02:46:03.93	+36:54:18.8	0.049	11.89	10.78	−25.70	1.38	n
Abell 399	02:57:53.13	+13:01:51.2	0.072	11.85	10.84	−26.43	6.40	n
Abell 401	02:58:57.78	+13:34:57.7	0.074	12.13	10.91	−26.42	9.94	n

Table A2. The $0.15 \lesssim z \lesssim 0.3$ WIRC BCGs. † denotes presence of H_α emission. y: H_α emission, n: no H_α emission.

Cluster	RA	Dec. (J2000)	z	J	K	M_K	L_X (10^{44}erg s^{-1})	$H_\alpha^\dagger$
Abell 115	00:56:00.24	+26:20:31.7	0.197	14.65	13.40	−25.91	14.59	y
Abell 1201	11:12:54.50	+13:26:08.9	0.169	14.45	13.16	−25.84	6.28	n
Abell 1204	11:13:20.52	+17:35:42.5	0.171	14.70	13.58	−25.44	7.26	y
Abell 1246	11:23:58.75	+21:28:47.3	0.190	14.99	13.67	−25.57	7.62	n
Abell 1423	11:57:17.38	+33:36:40.9	0.213	15.06	13.65	−25.81	10.03	n
Abell 1553	12:30:48.94	+10:32:48.4	0.165	13.71	12.60	−26.35	7.30	n
Abell 1682	13:06:45.82	+46:33:32.9	0.234	14.43	13.12	−26.54	11.26	n
Abell 1704	13:14:24.67	+64:34:32.2	0.221	14.79	13.56	−25.98	7.83	n
Abell 1758	13:32:38.59	+50:33:38.7	0.279	15.34	13.96	−26.05	11.68	n
Abell 1763	13:35:20.14	+41:00:03.8	0.223	14.44	13.11	−26.44	14.93	n
Abell 1835	14:01:02.06	+02:52:43.1	0.253	14.36	12.92	−26.89	38.53	y
Abell 1914	14:25:56.64	+37:48:59.4	0.171	14.09	12.85	−26.18	18.39	n
Abell 1961	14:44:31.82	+31:13:36.7	0.232	14.86	13.52	−26.11	6.60	–
Abell 2009	15:00:19.51	+21:22:10.6	0.153	14.02	12.83	−25.97	9.12	y
Abell 209	01:31:52.51	−13:36:41.0	0.209	14.46	13.07	−26.35	13.75	n
Abell 2111	15:39:41.81	+34:24:43.3	0.229	15.10	13.75	−25.86	10.94	n
Abell 2163	16:15:33.57	−06:09:16.8	0.203	14.98	13.24	−26.13	37.50	n
Abell 2218	16:35:49.39	+66:12:45.1	0.176	14.46	13.35	−25.73	9.30	n
Abell 2219	16:40:19.90	+46:42:41.4	0.226	14.70	13.34	−26.24	20.40	n
Abell 2254	17:17:45.91	+19:40:49.3	0.178	14.46	13.19	−25.92	7.73	n
Abell 2261	17:22:27.24	+32:07:57.9	0.224	14.04	12.62	−26.94	18.18	n
Abell 2445	22:26:55.80	+25:50:09.4	0.165	14.40	13.22	−25.73	4.00	–
Abell 2561	23:13:57.31	+14:44:21.9	0.163	14.71	13.53	−25.39	3.24	–
Abell 291	02:01:46.80	−02:11:56.9	0.196	15.42	14.10	−25.19	4.24	y
Abell 521	04:54:06.86	−10:13:23.0	0.248	14.86	13.53	−26.24	8.01	n
Abell 586	07:32:20.26	+31:38:01.9	0.171	14.36	13.13	−25.90	11.12	n
Abell 661	08:00:56.78	+36:03:23.6	0.288	14.84	13.53	−26.54	13.60	n
Abell 665	08:30:57.34	+65:50:31.4	0.182	14.92	13.69	−25.46	16.33	n
Abell 68	00:37:06.82	+09:09:24.3	0.255	14.94	13.51	−26.31	14.89	n
Abell 750	09:09:12.70	+10:58:27.9	0.180	14.36	13.05	−26.08	9.30	n
Abell 773	09:17:53.57	+51:44:02.5	0.217	14.64	13.22	−26.28	13.08	n
Abell 907	09:58:21.98	−11:03:50.3	0.153	14.50	13.18	−25.61	7.95	n
Abell 963	10:17:03.65	+39:02:52.0	0.206	14.31	12.94	−26.45	10.41	n
RX J1720.1+2638	17:20:10.08	+26:37:33.5	0.164	14.18	12.97	−25.97	6.66	y
RX J2129.6+0005	21:29:39.91	+00:05:19.7	0.235	14.64	13.27	−26.39	18.59	y
Zw 1432	07:51:25.15	+17:30:51.8	0.186	14.62	13.31	−25.88	5.27	y
Zw 1693	08:25:57.82	+04:14:48.7	0.225	14.62	13.24	−26.33	7.46	n
Zw 1883	08:42:55.99	+29:27:26.0	0.194	14.50	13.22	−26.05	6.41	y
Zw 2089	09:00:36.86	+20:53:41.2	0.230	15.50	14.10	−25.52	10.82	y
Zw 2379	09:27:10.68	+53:27:33.7	0.205	15.13	13.86	−25.53	5.71	y
Zw 2701	09:52:49.22	+51:53:05.8	0.214	14.70	13.40	−26.07	10.68	y
Zw 348	01:06:50.60	+01:04:10.1	0.255	15.21	13.78	−26.04	9.80	y
Zw 3916	11:14:27.43	58:22:43.5	0.206	15.11	13.80	−25.60	6.41	y
Zw 5247	12:34:17.45	+09:45:59.4	0.195	14.69	13.41	−25.87	10.12	n
Zw 5768	13:11:46.22	+22:01:37.2	0.266	14.33	13.08	−26.84	11.64	–
Zw 7215	15:01:23.09	+42:20:39.8	0.292	15.57	14.12	−25.98	11.26	n

Table A3. The $z \gtrsim 0.3$ MACS and archival BCGs.

Cluster	RA	Dec. (J2000)	z	J	K	M_K	L_X (10^{44} erg s^{-1})
MACS J0018.5+1626	00:18:33.68	+16:26:15.1	0.541	16.87	15.35	−26.08	18.74
MACS J0025.4−1222	00:25:27.44	−12:22:28.3	0.478	17.37	15.70	−25.46	12.40
MACS J0150.3−1005	01:50:21.24	−10:05:29.6	0.363	0.00	13.90	−26.66	7.83
MACS J0257.6−2209	02:57:09.78	−23:26:09.8	0.504	16.38	14.77	−26.50	15.40
MACS J0329.6−0211	03:29:41.68	−02:11:48.9	0.451	0.00	14.13	−26.89	13.85
MACS J0404.6+1109	04:04:32.71	+11:08:03.5	0.358	0.00	13.82	−26.71	14.75
MACS J0429.6−0253	04:29:36.14	−02:53:08.3	0.397	0.00	13.58	−27.17	16.61
MACS J0454.1−0300	04:54:11.13	−03:00:53.8	0.550	16.87	15.29	−26.18	16.86
MACS J0647.7+7015	06:47:51.45	+70:15:04.4	0.584	16.63	14.87	−26.74	21.70
MACS J0744.8+3927	07:44:51.98	39:27:35.1	0.686	17.21	15.33	−26.64	25.90
MACS J1359.8+6231	13:59:54.32	+62:30:36.3	0.330	0.00	14.32	−26.03	8.83
MACS J2050.7+0123	20:50:43.12	+01:23:29.4	0.333	0.00	14.67	−25.70	7.24
MACS J2129.4−0741	21:29:26.35	−7:41:33.5	0.570	17.29	15.57	−25.98	16.40
MACS J2214.9−1359	22:14:56.51	14:00:17.2	0.495	16.38	14.71	−26.52	17.00
MACS J2241.8+1732	22:41:56.18	+17:32:12.1	0.317	0.00	14.39	−25.88	10.10
MACS J2245.0+2637	22:45:04.62	+26:38:05.2	0.301	0.00	14.03	−26.14	13.62
RCS0224−0002	02:24:00.00	−0:02:00.0	0.770	0.00	16.87	−25.35	0.70
MS1054−0321	10:57:00.20	−03:37:27.4	0.830	17.70	15.99	−26.38	23.30

This paper has been typeset from a TEX/LATEX file prepared by the author.